Agonist-induced functional analysis and cell sorting associated with single-cell transcriptomics characterizes cell subtypes in normal and pathological brain

Sara Castagnola,[1] Julie Cazareth,[1] Kevin Lebrigand,[1] Marielle Jarjat,[1] Virginie Magnone,[1] Sébastien Delhaye,[1] Frederic Brau,[1] Barbara Bardoni,[2] and Thomas Maurin[1]

[1]*Université Côte d'Azur, CNRS, Institute of Molecular Cellular Pharmacology, F-06560 Valbonne, France;* [2]*Université Côte d'Azur, INSERM, CNRS, Institute of Molecular Cellular Pharmacology, F-06560 Valbonne, France*

To gain better insight into the dynamic interaction between cells and their environment, we developed the agonist-induced functional analysis and cell sorting (aiFACS) technique, which allows the simultaneous recording and sorting of cells in real-time according to their immediate and individual response to a stimulus. By modulating the aiFACS selection parameters, testing different developmental times, using various stimuli, and multiplying the analysis of readouts, it is possible to analyze cell populations of any normal or pathological tissue. The association of aiFACS with single-cell transcriptomics allows the construction of functional tissue cartography based on specific pharmacological responses of cells. As a proof of concept, we used aiFACS on the dissociated mouse brain, a highly heterogeneous tissue, enriching it in interneurons by stimulation with KCl or with AMPA, an agonist of the glutamate receptors, followed by sorting based on calcium levels. After AMPA stimulus, single-cell transcriptomics of these aiFACS-selected interneurons resulted in a nine-cluster classification. Furthermore, we used aiFACS on interneurons derived from the brain of the *Fmr1*-KO mouse, a rodent model of fragile X syndrome. We showed that these interneurons manifest a generalized defective response to AMPA compared with wild-type cells, affecting all the analyzed cell clusters at one specific postnatal developmental time.

[Supplemental material is available for this article.]

The selection, cloning, and morphological/functional characterization of individual cells in a suspension or from a tissue is a fastidious and lengthy procedure, despite several techniques, including limiting dilutions, laser microdissection (Datta et al. 2015), cytoplasm aspiration (Cadwell et al. 2016; Fuzik et al. 2016), microfluidics (Pollen et al. 2014; Zeisel et al. 2015; Tasic et al. 2016), and flow cytometry (Fulwyler 1965), having been set up to reach this goal. The latter is a robust and powerful technique that allows fast analysis and sorting of cell subsets from an initial heterogeneous sample. Cells can be sorted according to various parameters and are amenable to further characterization by single-cell RNA-sequencing (scRNA-seq) or mass spectrometry. Single-cell transcriptomics is a unique tool that provides precise and simultaneous analysis of the expression levels of thousands of genes in a complex heterogeneous population at the single-cell level (Poulin et al. 2016). Applied to the study of a pharmacological stimulation, this technique can discriminate homeostatic gene regulation at the tissue level from the modulation of the abundance of a given cell population, a phenomenon that is widely observed during development (Poulin et al. 2016; Ofengeim et al. 2017).

Coupling flow cytometry analysis and cell sorting with single-cell transcriptomics makes it possible to link a cell phenotype to its genotype, providing direct access to the molecular cues of a given phenotype. In this context, the key point is to submit the cells under analysis to the same stimulus. Functional fluorescence-activated cell sorting (FACS) analysis of intracellular pH or calcium variations using fluorescent probes (Chow et al. 2001; Vines et al. 2010) commonly consists of adding a stimulation (e.g., drugs or osmotic variations) into the sample tube containing the stained cell suspension before analysis or sorting. Although it takes up to 30 sec for the sample to reach the flow cell (the chamber aligning the cells in order to pass one-by-one through the laser beam for sensing), it can be considered that the fluorescence signal is measured "*at equilibrium*," as its detection and the physiological stimulus are temporally far from each other. This lag time prevents a comparable and accurate analysis of cell-to-cell calcium variations in commercial flow cytometers compared with the efficient sampling of calcium imaging (from a few milliseconds to seconds) obtained via fluorescence microscopy by combining the quick local delivery of drugs with high recording rates. As the cell suspension in the sample tube is currently injected under pressure into the cytometer fluidics in many commercial flow cytometers, the sample tube has to be removed to study cellular responses to drug stimulations. This manual step increases the time lag contributing to the observation of "stationary" cellular responses.

Corresponding author: bardoni@ipmc.cnrs.fr
Article published online before print. Article, supplemental material, and publication date are at http://www.genome.org/cgi/doi/10.1101/gr.262717.120.

Moreover, this methodology presumes that the first and last cells analyzed in the tube behave in an equivalent manner. With the appearance of sample lines using peristaltic pumping in commercial FACS (i.e., sample tube at atmospheric pressure), technical approaches have been proposed to add drugs to the cells in a continuous manner (Vines et al. 2010; Arnoldini et al. 2013). Although the time lag corresponding to the tube removal was suppressed, all cells remained simultaneously exposed to the drug but got analyzed at different times. Encouraging approaches to fast calcium response measurements by flow cytometry have been proposed in the past based on a fluidic modification in a FACS analyzer (Tárnok 1996; Zwartz et al. 2011). A method to monitor fast kinetics and the possibility of sorting the cells by modifying the tubing configuration of a FACStar Plus cytometer was also described (Dunne 1991). However, no sorting evidence was shown. These approaches remained in the form of prototypes and were only used for analysis.

The agonist-induced functional analysis and cell sorting (aiFACS) prototype we developed was built on a FACSAria III as an add-on. It allows the analysis of all the aforementioned parameters and also sorts cells according to their immediate and individual responses to a stimulus. We used it to analyze neurons derived from mouse brains, and obtained enriched preparations of interneurons. Further application of aiFACS to *Fmr1*-KO mice—a rodent model of fragile X syndrome (FXS)—brains, associated with single-cell RNA-seq, highlighted the functional and molecular impairment of interneurons in this disease. Besides the brain, aiFACS can be used to analyze cell populations of normal and pathological tissues, including tumors.

Results

Setup of aiFACS

We designed the aiFACS prototype for sorting cells according to their responses to a pharmacological stimulation monitored in real time with a fluorescent calcium indicator (Fig. 1A). The sorter fluidics system (BD FACAria III) was modified to allow drug injection into the sample line. Tubing (Fig. 1A, in red) with a diameter of 0.19 mm, equivalent to that of the sample line (Fig. 1A, in blue), was connected to two syringes upstream of the solenoid valve and the flow cell via a "Y" connector. Two valves alternatively opened

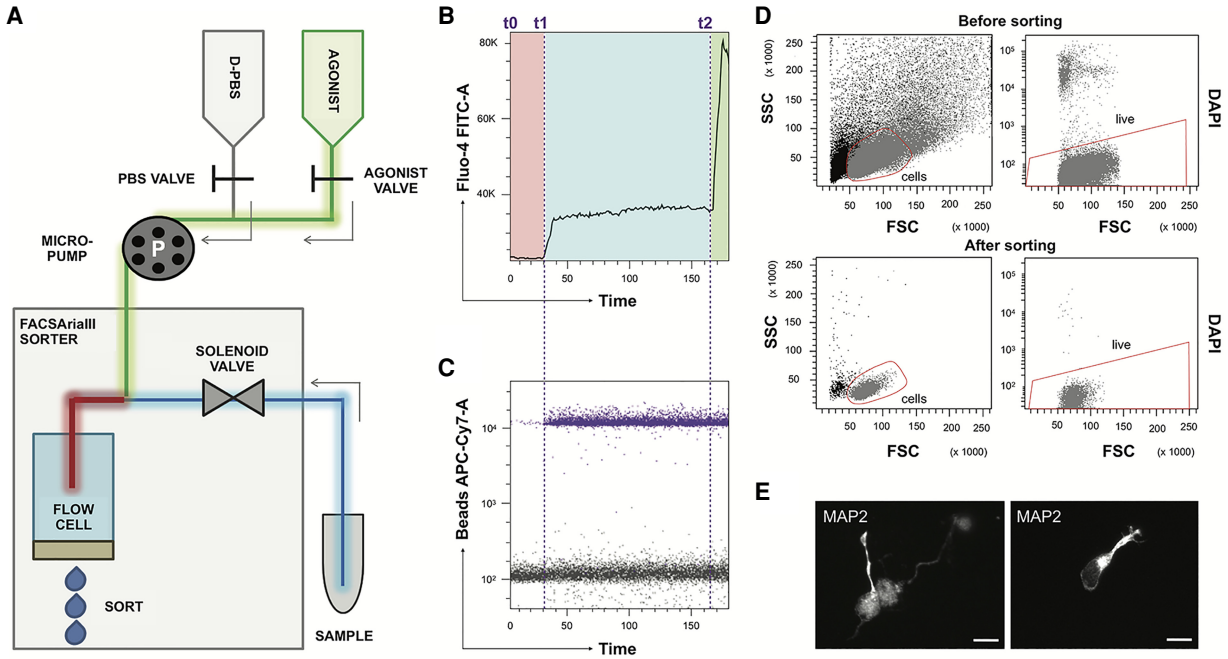

Figure 1. The aiFACS technique. (*A*) Schema of the instrumental apparatus: BD FACSAria III implemented with the aiFACS device. The sorter fluidics is modified to allow the injection of a pharmacological agonist. Two syringes, one containing D-PBS (in gray) and the other one containing the agonist (in green), are connected to their respective tubing: the D-PBS tubing (in gray) and the agonist tubing (in green). These are further connected to a downstream Y-shaped connector that enters the flow cell (the chamber in which the cells are aligned to pass one-by-one through the light beam for sensing). The sample is connected to the sorter through a tubing (in blue) having the same diameter as the agonist tubing (in green). A peristaltic micropump (P) allows control of the speed of solution injection and synchronization to the speed of sample flow in the sorter. The incubation time between each cell of the sample and the agonist is also controlled (red tubing). (*B*) Time versus Fluo-4 AM biparametric graph showing the response of the cells to different stimuli in real time. At time t0, the opening of the D-PBS valve starts the perfusion, and the baseline levels of fluorescence (in the red rectangle) are obtained with continuous perfusion. At time t1, the D-PBS valve is closed, and the one of the agonist is opened. The magnitude of the cellular calcium response to the KCl agonist (65 mM final) is shown in the light-blue rectangle. At time t2, ionomycin is added (6.5 μm final) to KCl as a positive control of stimulation. The maximal response of the cells is displayed in the green rectangle. (*C*) Addition of beads to the agonist solution allows real-time detection of the agonist presence. Bead fluorescence is shown in purple. (*D*) aiFACS allows viable recovery of stimulated cells. (*Upper* panels) Discrimination of cells based on scatter parameters ([FSC] forward scatter; [SSC] side scatter) before sorting (55.3% of the total population; *left* panel). The presort viability is determined by labeling the cells with DAPI (95.5% of the cells in the red region; *right* panel). (*Lower* panels) Discrimination of cells based on scatter parameters (FSC and SSC) after sorting (90.9% of the total population; *left* panel). The viability of the cells after KCl stimulation and aiFACS sorting is determined by reanalyzing the DAPI staining (99.7% of the cells in the red region; *right* panel). (*E*) Sorted neurons are viable and can grow neurites when plated on L-ornithine–coated glass coverslips, cultivated for up to 6 d in vitro (DIV 6) in complete neurobasal medium, and analyzed by immunocytochemistry (MAP2 staining). 63× magnification; scale bars, 10 μm.

or closed to control the injection syringes containing PBS and agonist and allowed the injection buffer to be selected. The speed of injection of the solutions was controlled using a peristaltic micropump to synchronize it with the FACS flow rate. The incubation time between each cell and the drug was, thus, strictly controlled (Fig. 1A, red tubing). At basal conditions, a sample resuspension buffer (D-PBS) was infused. To induce stimulation, the experimental drug was injected at 1.6× concentration. The cells were sorted according to their response to the drug. The precise dilution of the agonist was determined by the flow rates of the instrument and the pump. Its calibration was possible by using bead solutions of known concentrations (PE and APCCY7, respectively) instead of sample and agonist and by counting them at different flow rates, as shown in Supplemental Figure S1.

Using the Miltenyi neuron isolation kit (Holt and Olsen 2016; Berl et al. 2017), fresh postnatal day (PND) 18 adult mouse brains were dissociated to obtain RNA from the neuronal and nonneuronal populations, which were used to measure the expression of several neuronal (*Gad2*, *Itpr1*, *NeuroD1*, and *Nrg*) markers by RT-qPCR. This fraction was depleted in microglia (*Grn*), immature neurons (*Sox2*), astrocytes (*Gfap*), oligodendrocytes (*Mog2* and *Mbp*), and endothelial cells (*Rapgef4*) (Supplemental Fig. S2).

We injected neurons labeled with Fluo-4 AM to monitor the calcium response, and set up the machine using the parameters indicated in red in Supplemental Figure S3A. In the first step, based on our previous experience with ratiometric calcium imaging (Castagnola et al. 2018), we used KCl (65 mM final) as the agonist to elicit calcium entry into cells. We added fluorescent beads to monitor agonist perfusion and the increase in K^+ ion concentration in the sample line. D-PBS perfusion started at time t0 and stopped at time t1, when the KCl perfusion was initiated (Fig. 1B). Each cell was in contact with KCl for 3.2 sec (Supplemental Fig. S3A). The appearance of the beads corresponded to the arrival of cells stimulated with KCl in the flow cell (Fig. 1C). The increased level of calcium is shown in Supplemental Figure S3B. To verify the amplitude of the neuronal response and to have a positive control of stimulation, ionomycin was added to KCl at time t2 (Fig. 1B). Presort viability was determined by labeling dissociated neurons with DAPI staining (Fig. 1D). The viability of the cells that responded to KCl and after sorting by aiFACS was monitored using the previous labeling and was determined through reanalysis of the cells (Fig. 1D). Post-aiFACS KCl-responsive cells were viable (>90%) and capable of growing neurites when seeded on ornithine-coated glass coverslips (Fig. 1E). The gating strategy is detailed in the Methods section, and the various steps are shown in Supplemental Figure S4. In our analysis, we focused on the cells that showed homogenous Fluo-4 AM staining: the gating-dependent cell population 1 (GD1) cells (Fig. 2A). To precisely quantify the response to the stimulation using intracellular calcium concentration changes, the "resting"/unstimulated/baseline fluorescence of the cell population should be as homogeneous as possible. Indeed, this point is critical for setting an activation "threshold" beyond which responding cells are sorted. Resting Ca^{2+} levels in the GD1 population, compared with the remaining cell population (GD2 cells), were less variable, allowing us to set this threshold (Fig. 2A; Supplemental Fig. S5). This cell population was not contaminated with microglia (Supplemental Figs. S2, S6A,B) and was enriched in *Gad2*- and *Calb2*-expressing cells compared with GD2 (Fig. 2B). This suggests that our strategy favored the selection of interneurons (Le Magueresse and Monyer 2013). Furthermore, by performing a selection of neurons, in parallel with the same sample, by aiFACS and classical FACS, we observed different kinetics of the calcium responses of GD1 cells (Supplemental Fig. S7).

aiFACS selection and characterization of AMPA-responding interneuron populations

To obtain a proof of concept that this new method allows the selection and study of neuronal populations using pharmacological stimulation, we decided to study the activation of ionotropic receptors by its agonist α-amino-3-hydroxy-5-methyl-4-isoxazolepropionic acid (AMPA). After brain dissociation, cells stained with Fluo-4 AM were gated based on their fluorescence. We injected the cells in the FACS, supplying the flow cell with neutral D-PBS (baseline condition). After 3 min of recording, we stimulated GD1 cells with an AMPA solution (130 μM final). In this case, each cell was in contact with the drug for 3.2 sec. Selected interneuron GD1 cells were used to carry out single-cell transcriptomics using the 10x Genomics Chromium and Illumina sequencing platforms. After quality control, we analyzed 2170 cells (1287 AMPA and 883 baseline), with a median unique molecular identifier (UMI) per cell of 6652. The canonical correspondence analysis (CCA) of the two aggregated samples led to the identification of nine cell clusters (Fig. 3A,B). The AMPA response of each cluster is illustrated in Figure 3C. Selection of the various markers was performed on the basis of previous publications (Zeisel et al. 2015, 2018; La Manno et al. 2016; Tasic et al. 2016; Paul et al. 2017; Mi et al. 2018; Rosenberg et al. 2018).

Selected GD1 cells were broadly split into inhibitory (*Dcx*, *Gad1*, *Gad2*, *Dlx6*, *Dlx1*, *Dlx5*, and *Dlx2*) and excitatory neurons (*Slc17a7*, *Slc17a6*, *Nrn1*, *Neurod1*, and *Neurod2*) (Fig. 3A,B). We identified two clusters of cycling progenitors (*Top2a*, *Ube2c*, *Mki67*, *Hmgb2*, and *Cenpf*) (Fig. 3A; Supplemental Fig. S8) already engaged in inhibitory (*Dlx1*, *Dlx5*, and *Dlx2*) or excitatory lineages (*Selm*,

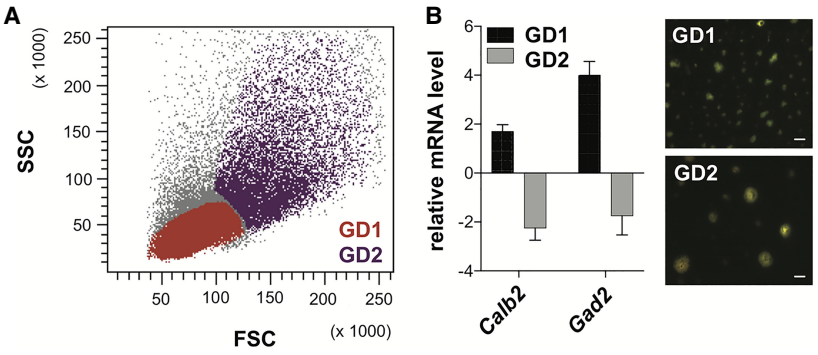

Figure 2. Gating-dependent cell populations. (*A*) Discrimination of cells based on scatter parameters: (FSC) forward scatter; (SSC) side scatter. Cells were gated according to their size/structure. (GD1) Gating-dependent cell population 1; (GD2) gating-dependent cell population 2. (*B*) RNA was purified from WT GD1 and GD2 cells. Neuronal and nonneuronal marker levels were analyzed in both populations by RT-qPCR. The graph (on the *left*) shows mRNA expression relative to the total WT neuron suspension (WT input). GD1 and GD2 cells were live-imaged 2 h after aiFACS sorting (on the *right*). 63× magnification; scale bars, 15 μm.

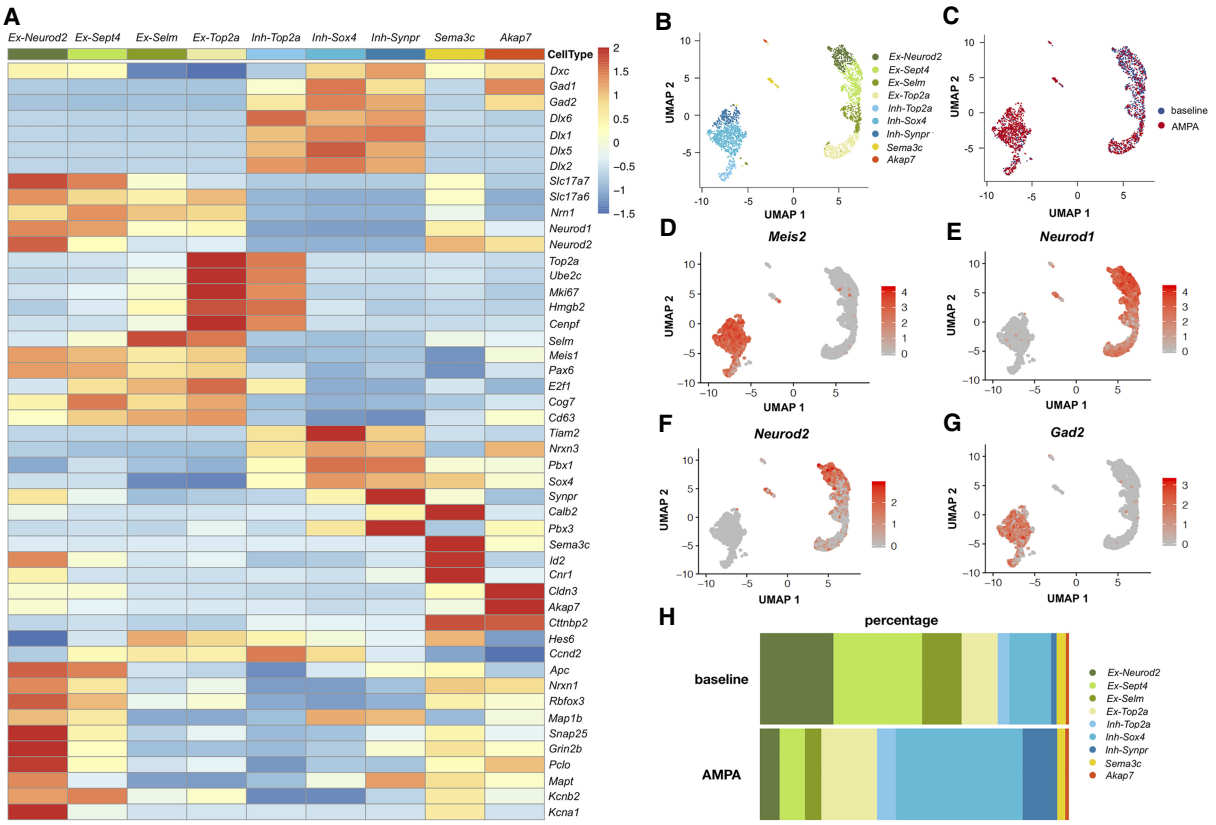

Figure 3. Single-cell transcriptomic analysis of GD1 cells. (*A*) Heatmap of marker gene expression for the nine identified cell clusters in the aggregated data set before and after stimulation. *Ex-Neurod2*, *Ex-Sept4*, *Ex-Selm*, and *Ex-Top2a*: excitatory clusters; *Inh-Top2a*, *Inh-Sox4*, and *Inh-Synpr*: inhibitory clusters; *Sema3c*: ependymal cells; *Akap7*: oligodendrocytes. (*B*) UMAP representation of the distribution of the nine clusters. (*C*) UMAP representation of the two aggregated WT samples: baseline and AMPA. (*D*) UMAP representation of the *Meis2*-expressing cell cluster. (*E*) UMAP representation of the *Neurod1*-expressing cell cluster. (*F*) UMAP representation of the *Neurod2*-expressing cell cluster. (*G*) UMAP representation of the *Gad2*-expressing cell cluster. (*H*) Relative proportion of cells by cluster type for individual samples at the baseline and after aiFACS selection.

Meis1, *Pax6*, *E2f1*, *Cog7*, and *Cd63*). Inhibitory neurons were split into three main populations that express *Meis2* in combination with other markers: *Tiam2*/*Nrxn3*, *Pbx1*/*Sox4*, and *Synpr*/*Calb2*/*Pbx3*. We also identified two inhibitory neuron clusters further advanced in their maturation process: "*Sema3c*" (*Calb2*, *Sema3c*, *Id2*, and *Cnr1*) composed of VIP neuron precursors, and inhibitory mature neurons composed of "*Rora*" cells (*Cldn3*, *Akap7*, *Cttnbp2*, *Gad1*, and *Gad2*) that may give rise to CCK neurons (Fig. 3A,B, G). Next, we identified a continuum of three excitatory cell clusters, separated by their differentiation status: ventricular zone or dentate gyrus granule cell intermediate progenitors (*Hes6* and *Ccnd2*), and two clusters of further differentiated cells (*Neurod1*, *Neurod2*, *Apc*, *Nrxn1*, *Rbfox3*, and *Map1b*), which could be split according to their intermediate or final maturation, as indicated by the expression of pre- and postsynaptic (*Snap25*, *Grin2b*, and *Pclo*), cytoskeletal (*Mapt*), and potassium channel (*Kcnb2 or Kcna1* and *Kcnk2*) markers (Fig. 3A,B). The distribution of some specific markers (*Meis2*, *Neurod1*, *Neurod2*, and *Gad2*) is shown in the context of various clusters (Fig. 3D–G). In Figure 3H, the comparison of cell clusters before and after aiFACS selection is shown. In particular, the post-aiFACS selection clearly shows that AMPA stimulation promoted the positive selection of *Meis2* interneurons (12%–38% of sorted cells) (Fig. 3B,D,H).

In summary, aiFACS is a tool to analyze a tissue response to a pharmacological stimulation, offering new information on ion homeostasis players and the cellular specificities that drive the heterogeneity of the cell response.

aiFACS selection through AMPA stimulation unveils impaired interneurons in *Fmr1*-KO mouse brain

To validate that aiFACS is helpful for studying brain disorders, we applied it to dissociated neurons from mouse *Fmr1*-KO brains. This disorder is owing to the lack of function of the FMRP translational regulator 1 (FMR1) protein. Indeed, recent studies have highlighted interneuron dysfunctions in FXS (Olmos-Serrano et al. 2010; Le Magueresse and Monyer 2013; Patel et al. 2013; Cea-Del Rio and Huntsman 2014; Goel et al. 2018; Yang et al. 2018), as well as alterations in the expression, trafficking, and functioning of AMPA receptors (Cheng et al. 2017). To carry out this part of the study, we implemented the technique by introducing a dynamic selection to simultaneously analyze wild-type (WT) and *Fmr1*-KO samples. We dissociated PND 18 WT and *Fmr1*-KO brains, and cells from both genotypes were stained with Fluo-4 AM. WT cells were further labeled with Alexa-Fluor 594-coupled wheat germ agglutinin (WGA 594), whereas *Fmr1*-KO cells were labeled with Alexa-Fluor 647 WGA. This labeling allowed the mixing of cells of both genotypes to perform a combined analysis (Fig. 4A), and did not influence the selection (Supplemental Fig. S9). Following the previous

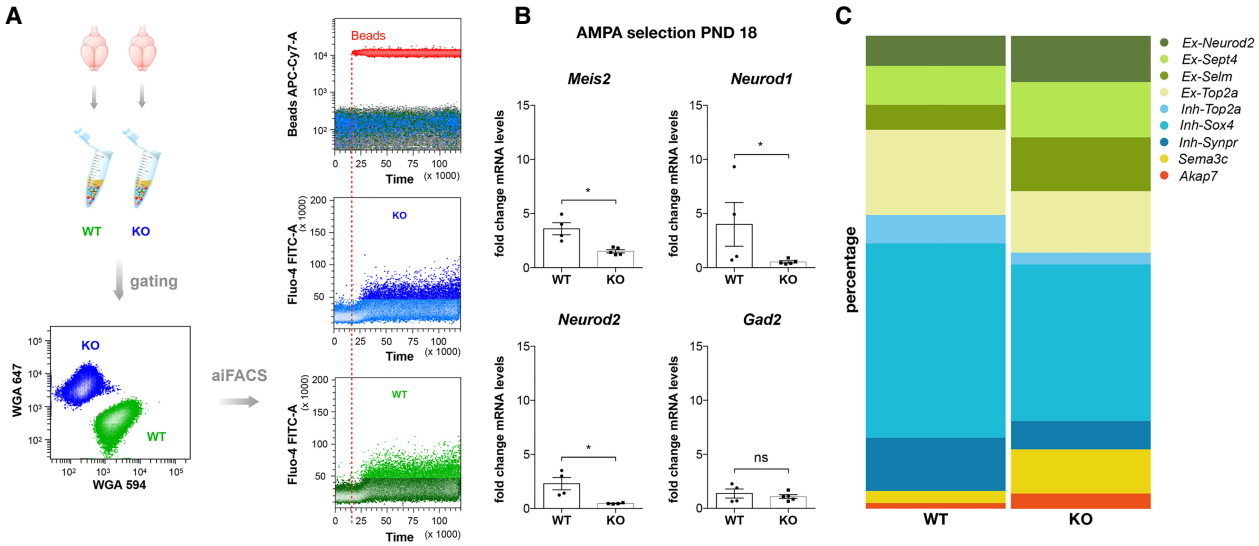

Figure 4. aiFACS multiplex analysis. (*A*, *left*) PND 18 WT and *Fmr1*-KO brains were dissociated, and neuronal cells were selected. Neurons from both genotypes were multiplexed by fluorescent labeling with wheat germ agglutinin (WGA; WGA647 for WT, and WGA594 for *Fmr1*-KO) and were processed and analyzed simultaneously. (*Upper right* panel) The injection of fluorescently labeled beads simultaneously with AMPA (130 μM final) perfusion allows the monitoring of the agonist in the flow cell. (*Central*, *lower* panels) Real-time monitoring of neuronal responses to AMPA stimulation by Fluo-4 AM fluorescence quantification in *Fmr1*-KO (blue) and WT (green) cells. (*B*) mRNA was purified from 5000 GD1 cells, and inhibitory and excitatory marker expression levels were quantified by RT-qPCR and compared for WT and *Fmr1*-KO. Marker expression upon AMPA stimulation at PND 18 in both genotypes is presented as the fold change respective to the expression of WT neurons subjected to aiFACS (input WT). Results are presented as the mean ± SEM, Mann–Whitney *U* test; (*) $P < 0.05$; (ns) not significant. For *Meis2*, *Neurod1*, and *Gad2*: WT, $n = 4$; *Fmr1*-KO, $n = 5$. For *Neurod2*: WT, $n = 4$; *Fmr1*-KO, $n = 4$. Each *n* corresponds to two (nonlittermate) mouse brains and is the mean of two independent replicates. (*C*) Percentage of cells belonging to the nine clusters after single-cell analysis of AMPA response in WT and *Fmr1*-KO GD1 cells. *Ex-Neurod2*, *Ex-Sept4*, *Ex-Selm*, and *Ex-Top2a*: excitatory clusters; *Inh-Top2a*, *Inh-Sox4*, and *Inh-Synpr*: inhibitory clusters; *Sema3c*: ependymal cells; *Akap7*: oligodendrocytes.

procedure, we selected 5000 cells for each condition (baseline and AMPA stimulation).

Because upon AMPA stimulation GD1 cells were strongly enriched in *Meis2*-expressing cells, we measured the expression levels of *Meis2* by RT-qPCR after AMPA stimulation of both WT and *Fmr1*-KO GD1 cells obtained from new sets of animals by evaluating the fold change respective to the expression of aiFACS-selected WT neurons (Fig. 4B). Our results showed that the AMPA-responding GD1 *Fmr1*-KO neurons expressed lower levels of *Meis2*, *Neurod1*, and *Neurod2* mRNA compared with WT neurons, whereas no changes were observed for *Gad2* (Fig. 4B). This suggests that AMPA-responding *Fmr1*-KO GD1 cells display abnormal expression levels of the analyzed genes compared with WT or that a different number of cells express these markers in WT and *Fmr1*-KO. To gain a deeper insight into this phenomenon, we performed single-cell sequencing on AMPA-stimulated GD1 cells dissociated from *Fmr1*-KO brains. We analyzed 1047 *Fmr1*-KO GD1 cells with a median UMI per cell of 6585. mRNA targets of FMR1 selected by high-throughput sequencing of RNA isolated by cross-linking immunoprecipitation (HITS-CLIP) (Maurin et al. 2018) were identified in each cluster. We used the top 200 prominent mRNA targets to calculate a signature score (i.e., a composite expression score of a set of genes using Seurat's AddModuleScore function using standard parameters) (Butler et al. 2018; Stuart et al. 2019). This score is plotted as a boxplot per cell type (WT/KO sample aggregates) (Supplemental Fig. S10). We identified the same cell clusters present in AMPA-stimulated WT GD1 cells, even if their proportions were altered (Fig. 4C). This suggests an overall impairment in AMPA response in the absence of FMR1, as cells from each cluster are affected. This variability could be explained by the different levels of maturity or developmental profile of the cells comprising each cluster in WT versus *Fmr1*-KO brains.

To evaluate this hypothesis, we measured the levels of the analyzed markers at baseline (Fig. 5A) by using new sets of nonlittermate PND 18 and PND 19 WT, and *Fmr1*-KO mouse neuronal populations subjected to aiFACS. RT-qPCR analysis revealed elevated expression levels of the two proneuronal genes *Neurod1* and *Neurod2* in *Fmr1*-KO baseline GD1 cells. To assess whether the phenotype we observed was associated with the developmental process, we repeated the analysis in mice older than PND 18. At PND 19, RT-qPCR analysis indicated that the expression levels of *Meis2*, *Neurod1*, *Neurod2*, and *Gad2* did not show a significantly different abundance between the two genotypes (Fig. 5B). Consistently, the analysis of PND 19 GD1 *Fmr1*-KO neurons revealed that their response to AMPA was unchanged compared with WT neurons for all the analyzed markers (Supplemental Fig. S11). We can therefore suggest that AMPA-responding *Fmr1*-KO cells might be altered at this stage of development, at least for the GD1 population expressing these markers.

Discussion

A new approach to study pharmacological cell responses

We developed the aiFACS prototype with the aim of exploring the cell-specific responses to environmental and pharmacological stimuli, particularly for fast kinetic studies. Classical FACS analysis does not allow the sorting of living cells, which are all subjected to the same brief stimulus. Our technique showed feasibility of calcium monitoring in real time with a fluorescent indicator, as well as sorting of cells according to their calcium response upon

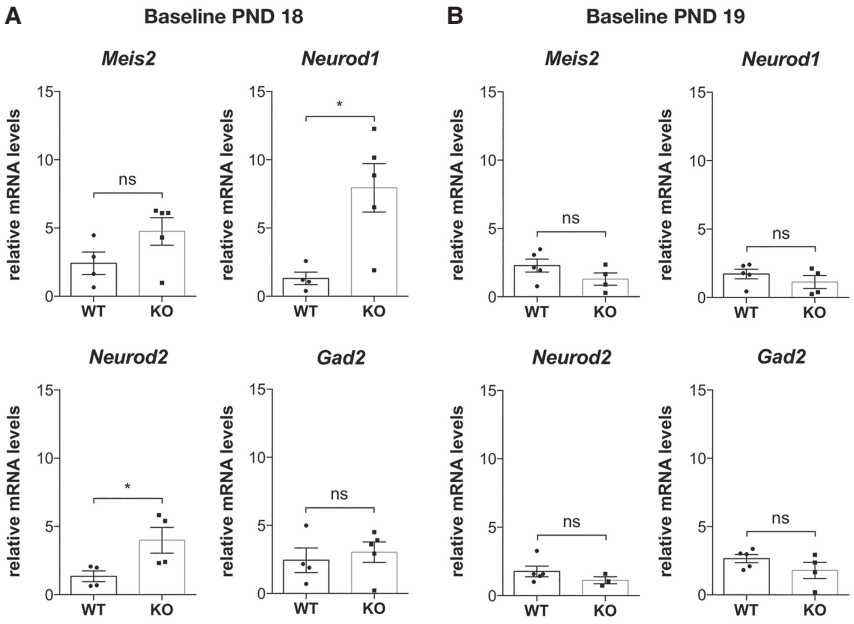

Figure 5. Baseline gene expression at PND 18 and PND 19. (*A*) At PND 18, mRNA was purified from 5000 GD1 cells; inhibitory and excitatory marker expression levels were quantified by RT-qPCR and compared between WT and *Fmr1*-KO brains. Baseline marker expression in both genotypes is presented respective to the expression of WT neurons subjected to aiFACS (input WT). Results are presented as the mean ± SEM, Mann–Whitney *U* test; (*) $P < 0.05$; (ns) not significant. For *Meis2*, *Neurod1*, and *Gad2*: WT, $n = 4$; *Fmr1*-KO, $n = 5$. For *Neurod2*: WT, $n = 4$; *Fmr1*-KO, $n = 4$. Each *n* corresponds to two (nonlittermate) mouse brains and is the mean of two independent replicates. (*B*) At PND 19, mRNA was purified from 5000 GD1 cells, and inhibitory and excitatory markers expression levels were quantified by RT-qPCR and compared between WT and *Fmr1*-KO brains. Baseline marker expression in both genotypes is presented respective to the expression of WT neurons subjected to aiFACS (input WT). Results are presented as the mean ± SEM, Mann–Whitney *U* test; (ns) not significant. For *Meis2*, *Neurod1*, and *Gad2*: WT, $n = 5$; *Fmr1*-KO, $n = 4$. For *Neurod2*: WT, $n = 5$; *Fmr1*-KO, $n = 3$. Each *n* corresponds to two (nonlittermate) mouse brains and is the mean of two independent replicates.

pharmacological treatment. The entry of calcium into neurons is a tightly controlled process. This is owing to the opening of Ca^{2+} permeable channels, which are known to respond to a large array of stimuli, such as membrane depolarization or extracellular chemical messengers, that can directly activate the channel or can act indirectly via intracellular molecular signaling (Barritt 1999; Taylor 2002). In particular, fast and brief increases in intracellular calcium levels are known to be involved in various steps of neuronal development. These calcium transients play a pivotal role in the regulation of neurotransmitter phenotypes, dendritic morphology, axonal growth, and guidance (Rosenberg and Spitzer 2011). Modulation of all these parameters is critical for neuronal subtype specification. Hence, the duration and quality of the stimulus are the most critical aspects to manage while setting up the aiFACS method, because they represent the key modulators of the selection. Indeed, the duration of the stimulus was dependent on the length of the red tubing (Fig. 1A) and on the speed of the sample flow rate (Supplemental Fig. S3A), as mentioned previously by Tàrnok (1996) in their fixed-time flow cytometry approach. We decided to use a stimulus of 3.2 sec based on our previous studies using calcium imaging in cultured neurons. In those experiments, we observed a peak of intracellular calcium after 3.2 sec in cultured cortical neurons upon various stimuli (Castagnola et al. 2018). This controlled time is a critical point because a very long time of contact between the neurons and the agonist, owing to the long process of cell sorting by classical FACS (Supplemental Fig. S7), could result in the modification of neuronal gene expression. For instance, activation of CREB by phosphorylation was observed 1 min after Ca^{2+} stimulation (Bito et al. 1996). Moreover, aiFACS allows the application of one or more stimuli to the same cells under analysis in a subsequent manner, as shown in Figure 1 for KCl and ionomycin. aiFACS-selected cells can be analyzed by various downstream methods, including scRNA-seq. This technique allows us to unravel cell identity, define the molecular determinants of the pharmacological response, and directly assess gene expression differences, including splice variants and edited transcripts. Furthermore, by introducing dynamic selection, WT and one or more mutants can be analyzed simultaneously in the same run, or multiple individuals having the same genotype can be multiplexed and analyzed separately but simultaneously.

To appreciate the power of aiFACS, we analyzed the brain as a highly specialized and heterogeneous tissue. By applying this technique to PND 18 mouse brains, we showed the possibility of enriching our samples in interneurons responding rapidly to a pharmacological agonist. To date, the study of interneurons has been confined to restricted brain areas or circuits because of the limited availability of high-throughput analysis tools that allow a thorough and precise analysis of the complex molecular, spatial, anatomical, and connection heterogeneities of the brain (Le Magueresse and Monyer 2013). We are convinced that our approach will enable a novel function-based classification of interneuron cells rather than a classification based on (or in addition to) other parameters such as localization, morphology, and gene expression.

A proof of concept in FXS

We compared WT and *Fmr1*-KO aiFACS-selected cell responses to AMPA. Our results show a global altered AMPA response in *Fmr1*-KO cells, in agreement with other studies (Cheng et al. 2017). Based on RNA-seq profiles, the same clusters of cells were present, but their ratio was different between WT and *Fmr1*-KO cells. Indeed, we repeated aiFACS selection on additional sets of WT and *Fmr1*-KO mouse brains and validated that *Fmr1*-KO cells display abnormal levels of *Meis2*, *Neurod1*, and *Neurod2*, whereas consistent levels of *Gad2* were present (Fig. 4B). These data confirm that the balance of inhibitory/excitatory neuronal activity is abnormal in the FXS brain, as previously suggested (Contractor et al. 2015; Li et al. 2020). We discovered a specific deregulation of *Meis2* AMPA-responding interneurons in the *Fmr1*-KO brain. *Meis2* is a crucial transcription factor for interneuron maturation in the rodent brain. Mutations or deletions of this gene have been associated with neurodevelopmental disorders displaying intellectual disability and autism spectrum disorder (Verheije et al.

2019; Giliberti et al. 2020). *Meis2* is a marker of lateral ganglionic eminence-derived interneurons that are medium spiny neurons of the striatum. Moreover, *Meis2* interneurons are in the rostral migratory system, giving rise to dopaminergic periglomerular interneurons of the olfactory bulb (Allen et al. 2007; Agoston et al. 2014; Fujiwara and Cave 2016). *Meis2* interneurons were never involved in the pathophysiology of FXS, and altered levels of *Meis2* were never observed in the *Fmr1*-KO brain. Indeed, the previous analysis of cortex and hippocampus transcriptomics of the *Fmr1*-KO mice did not reveal substantial differences compared with WT samples (Maurin et al. 2018). Therefore, our data clearly show that aiFACS allows us to highlight unexpected impairments in cell subtypes by carrying out a sensitive functional cellular selection.

In summary, our results showed the presence of functional and molecular impairments in *Fmr1*-KO interneuron subtypes that are synchronized with brain development, and open up new research perspectives for FXS. We observed that the expression levels of some markers, such as the two proneural genes *Neurod1* and *Neurod2*, which are deregulated at PND 18, appear normalized when analyzed at PND 19. Even if a more detailed analysis is needed for a deeper understanding of postnatal neuronal development in *Fmr1*-KO mice (Tang et al. 2015; Maurin et al. 2019), we can consider that this difference in expression could be a consequence of an altered developmental profile of *Fmr1*-KO interneurons, dependent on the function of FMR1. This protein is known to modulate a network of pathways, including calcium signaling, which is supposed to be disorganized in its absence (Miyashiro et al. 2003; Richter and Coller 2015; Ferron 2016; Castagnola et al. 2018; Maurin and Bardoni 2018; Maurin et al. 2018).

aiFACS was developed on a simpler and similar basis to previous technical modifications on commercial flow cytometers designed to optimize real-time flow cytometry cellular assays in the past (Dunne 1991; Tárnok 1996; Vines et al. 2010; Zwartz et al. 2011; Arnoldini et al. 2013). Flow cytometers fluidics principally use two different technologies to inject the sample into the sheath fluid: by applying pressure on the sample tube or by peristaltic pumping. Some investigators (Dunne 1991; Tárnok 1996) used an approach similar to that described previously (Kelley 1989), with a derivation of the pressurization from the cytometer to create a stimulus line to mix drugs with the cells. Later, by using the Accuri C6 flow cytometer based on sample injection at atmospheric pressure, other investigators (Vines et al. 2010; Arnoldini et al. 2013) suggested simply adding the stimulation to the sample tube. Although simpler, the main drawback of the latter approach was in monitoring heterogeneous cellular stimulations, because the first and last cells monitored would be exposed to the drug for different lengths of time. If our aiFACS approach seems closer to the previous developments (Dunne 1991; Tárnok 1996), it offers the advantage of being more flexible in connecting a stimulus line to a commercial flow cytometer managing multiple drug injections and proving to be efficient with sorting strategies, whereas previous developments only showed cell analysis. This is a key aspect to perform further single-cell omics studies. The proof of concept on the FXS mouse model confirmed that aiFACS allows the collection of a wealth of new information concerning the molecular pathology of a brain disorder. This was possible by using both a sophisticated approach such as scRNA-seq and a simple and inexpensive technique such as RT-qPCR.

Our parameters and working conditions resulted in the study of interneurons. However, by modulating the aiFACS selection parameters, testing different developmental times, using various stimuli, and multiplying the analysis of readouts, we think that it will be possible to extend the use of aiFACS to other brain cell types and also to a large panel of normal and pathological tissues, including tumors. In perspective, aiFACS can be applied to study second messenger modulations, kinase activations, ionic fluxes, and many other biochemical and pharmacological mechanisms at the level of individual cells.

Methods

Animal handling and care

Animal care was conducted in accordance with the European Community Directive 2010/63/EU. WT and *Fmr1*-KO mice on a C57BL/6J congenic background were obtained from Prof. R. Willemsen (*Fmr1*-KO line 2) (Mientjes et al. 2006). All animals were housed in groups of six under standard laboratory conditions (22°C, 55 ± 10% humidity, 12-h light/12-h dark diurnal cycles) with food and water provided ad libitum. Only the brains of male animals were analyzed. For timed pregnancies, noon on the day of the vaginal plug was counted as E0.5. The experiments were performed following the Animals in Research: Reporting In Vivo Experiments (ARRIVE) guidelines (Kilkenny et al. 2010; https://arriveguidelines.org/publications). The experiments were approved by our local ethics committee and the Ministry of Education and Research (approval no. 00788.01).

Brain dissociation and neuron isolation

Full brains were dissected from PND 18 mice. A brief wash with complete D-PBS (supplemented with 0.5% bovine serum albumin, 1% pyruvate, and 15 mM glucose) was performed before cutting the brains in six equally thick sagittal sections (2 mm), using a mouse brain matrix slicer (CellPoint Scientific) and razor blades. Brain slices were dissociated using a gentleMACS octo dissociator and the adult brain dissociation kit (Miltenyi Biotec) following the manufacturer's instructions. The neuron isolation kit (Miltenyi Biotec) was used for magnetic selection of neuronal cells.

Neuron labeling

WT and *Fmr1*-KO neuronal suspensions were labeled with a combination of the Fluo-4 AM calcium indicator (5 µg/mL; Invitrogen) and either Alexa-Fluor 594-coupled WGA or Alexa-Fluor 647-coupled WGA (5 µg/mL; Invitrogen) in D-PBS for 20 and 10 min, respectively, at 37°C. The dyes were switched in each experiment. Centrifugation at 300*g* for 10 min at room temperature was performed subsequently, and the cells were resuspended in 300 µL of D-PBS. Before sorting, neurons were labeled with 0.05 µg/mL DAPI.

aiFACS and cell sorting

Cells were sorted using a 100-µm nozzle, on a FACSAria III (BD Biosciences) equipped with four lasers. Fluo-4 AM, Alexa Fluor 594, DAPI, Alexa Fluor 647, and APC-Cy7 were excited at 488 nm, 561 nm, 405 nm, and 633 nm, respectively, and detected using BP530/30, BP610/20, BP450/40, BP660/20, and BP780/60 filters. The sorter was implemented with a homemade injection system (Fig. 1A). The sample line was improved, upstream of the solenoid valve, with an injection system composed of two syringes controlled by valves and a peristaltic micropump. D-PBS was placed in the first syringe. A 1.6× concentrated agonist solution (100 mM KCl, 200 µM AMPA, or 10 µM ionomycin) was prepared, and APC-CY7–labeled CompBead compensation particles (BD Biosciences) were added to the solution before putting it in the

second injection syringe. Both the MINIPULS 3 peristaltic pump (Gilson) and the cytometer flow rate were set to 39 µL/min. Baseline acquisition and sorting were performed with the valve of the buffer syringe opened. Once the valve of the agonist syringe was opened, the valve of the buffer syringe was closed. The agonist solution running in the flow cell was monitored by the appearance of the beads. At this point, the agonist-responding cells started to be sorted. Cells were collected in D-PBS. Data were analyzed using BD FACSDiva v6 and FlowJo softwares (BD Biosciences).

Gating strategy

Cells and beads were identified by their size/structure profiles. The first region, cells, was drawn around the GD1 population. Next, living cells were identified as DAPI-negative. Doublets were excluded based on morphological parameters: side scattered (SSC) and forward scattered (FSC). Among the living cells, in singlets, a graph of the fluorescence of WGAs coupled either to Alexa Fluor 594 (605/40 channel) or to Alexa Fluor 647 (APC channel) allowed us to identify the cells from each mouse phenotype. For each mouse, the basal level of Fluo-4 AM was represented as a function of cell size. A region above this baseline was defined and used for identifying the cells that responded to the agonist in order to sort them. The appearance of the beads gave the signal for the start of the stimulation and, thus, the sorting (Supplemental Fig. S4).

RNA preparation and RT-qPCR

Total RNA was extracted from aiFACS-sorted cells using TRIzol reagent (Sigma-Aldrich) according to the manufacturer's instructions. In each experimental sample, 1 µg of RNA (Supplemental Fig. S2) or 5000 cells (Figs. 2B, 4B, 5A,B; Supplemental Fig. S11) were used for each condition. RNA was purified using 500 µL of TRIzol reagent (Sigma-Aldrich) and precipitated from the aqueous phase with 500 µL of isopropanol (VWR Medicals) and 1 µL of glycogen (20 µg/µL, Invitrogen). RNA was resuspended in 20 µL (Supplemental Fig. S2) or 11 µL (Figs. 2B, 4B, 5A,B; Supplemental Fig. S11) of nuclease-free H_2O. Either 1 µg (Supplemental Fig. S2) or 11 µL (Figs. 2B, 4B, 5A,B; Supplemental Fig. S11) of RNA was added to the RT reaction that was performed using the SuperScript IV synthesis kit (Invitrogen). Initial amplification was performed with a denaturation step for 5 min at 65°C, followed by oligo(dT) annealing for 10 min at 23°C, primer annealing for 10 min at 53°C, and primer extension for 10 min at 80°C. Upon completion of the cycling steps, the reactions were stored at −20°C. Quantitative PCR (RT-qPCR) was performed on a light cycler 480 (Roche) with MasterMix SYBR Green (Roche) following the manufacturer's instructions and according to the MIQE guidelines (Bustin et al. 2009). Primer sequences are listed in Supplemental Table S1.

Immunofluorescence

aiFACS-sorted neurons were plated on ornithine-coated glass coverslips (35-mm diameter) and cultivated in complete medium: neurobasal (Invitrogen) supplemented with B-27 (Invitrogen) and GlutaMAX (Invitrogen) as previously described (Abekhoukh et al. 2017; Maurin et al. 2019). Neurons were fixed, and immunofluorescence was performed with microtubule associated protein 2 (MAP2) antichicken polyclonal antibody (BioLegend 822501) detected with a secondary goat antichicken Alexa 594 (Invitrogen A32759) 6 d after the selection, as previously described (Drozd et al. 2019). Fluorescent images were taken using a wide-field upright fluorescence microscope (Axioplan2, Carl Zeiss), with an ORCA ER CCD camera (Hamamatsu), through a rhodamine filter set (BP565/30; LP585; BP620/60) and a PlanApoChormat 63×/1.4 DIC oil immersion objective (pixel size: 100 nm).

Microglia were labeled as previously described (Cazareth et al. 2014) using the following antibodies: BV510 anti-mouse CD45-clone 30-F11 (BD Biosciences 563891) and AlexaFluor700 anti-mouse CD11b-clone M1/70 (Sony Biotechnology 1106110).

Droplet-based scRNA-seq

Single-cell suspensions were converted to barcoded scRNA-seq libraries using the Chromium Single Cell 3′ Library, Gel Bead & Multiplex Kit, and Chip Kit (10x Genomics), aiming for an estimated 2000 cells per library, following the manufacturer's instructions. Samples were processed using kits pertaining to the V2 barcoding chemistry of 10x Genomics. Libraries were sequenced using Illumina NextSeq 500 and mapped to the mouse genome (build mm10) using Cell Ranger (10x Genomics). Gene positions were annotated as per Ensembl build 84.

Single-cell gene expression quantification and determination of major cell types

Raw gene expression matrices, generated per sample using Cell Ranger (version 2.0.0), were loaded and processed in R (version 3.4.3) (R Core Team 2018). Samples were analyzed independently within the Seurat workflow using the Seurat R package (version 3.0.0) (Stuart et al. 2019). First, cells that had >95% dropouts were removed. Gene expression matrices from the remaining cells were normalized using SCTransform (Hafemeister and Satija 2019) from the Seurat package. To reduce the dimensionality of each data set, the resulting variably expressed genes were summarized by principal component analysis, and the first 30 principal components were further summarized using UMAP dimensionality reduction. The three samples from independent analyses were then integrated using CCA. The analysis workflow was then run on an integrated data set. Cell clusters in the resulting UMAP two-dimensional representation were annotated to known biological cell types using canonical marker genes described in the literature (Zeisel et al. 2015, 2018; La Manno et al. 2016; Tasic et al. 2016; Paul et al. 2017; Mi et al. 2018; Rosenberg et al. 2018).

Statistics

Statistical tests used in each experiment are indicated in the figure legends. Data are expressed as mean ± SEM, and *P*-values (or adjusted *P*-values) < 0.05 were considered statistically significant. Statistical analysis was performed using Prism Software version 7 (GraphPad Software).

Data access

The single-cell transcriptomic data generated in this study have been submitted to the NCBI Gene Expression Omnibus (GEO; https://www.ncbi.nlm.nih.gov/geo/) under accession number GSE142274. Data processing scripts (R code) and data used in this study are publicly available through the GitHub repository (https://github.com/ucagenomix/sc.castagnola.2020) and as Supplemental Code.

Competing interest statement

The authors declare no competing interests.

Acknowledgments

We thank M. Beal, M. Drozd, and M. Grossi for discussion, help, and encouragement and M. Capovilla and E. Lalli for critical reading of the manuscript. This study was supported by Institut national de la santé et de la recherche médicale (Inserm), Centre national de la recherche scientifique (CNRS), Université Côte d'Azur, Fraxa Research Foundation, Féderation Recherche sur le Cerveau, Fondation Jérôme Lejeune, and Agence Nationale de la Recherche ANR-11-LABX-0028-01, ANR-15-CE16-0015, and ANR-15-IDEX-0001. We acknowledge the "Microscopie Imagerie Côte d'Azur" (MICA) GIS-IBiSA multisite platform and the "UCAGenomiX platform" supported by Conseil Départemental 06, Région Provence-Alpes-Côte d'Azur (PACA), Fondation ARC pour Recherche sur le Cancer (ARC), Cancéropôle PACA, and Commissariat aux Grands Investissements ANR-10-INBS-09-03 and ANR-10-INBS-09-02.

Author contributions: T.M. conceived the study; B.B. and T.M. supervised the project; B.B., T.M., J.C., and F.B. designed the experiments; S.C., J.C., K.L., M.J., S.D., V.M., and T.M. acquired data; and S.C., J.C., K.L., F.B., T.M., and B.B. analyzed the data. S.C., B.B., and T.M. wrote the manuscript. All authors edited and provided critical inputs to the manuscript.

References

Abekhoukh S, Sahin HB, Grossi M, Zongaro S, Maurin T, Madrigal I, Kazue-Sugioka D, Raas-Rothschild A, Doulazmi M, Carrera P, et al. 2017. New insights into the regulatory function of CYFIP1 in the context of WAVE- and FMRP-containing complexes. *Dis Model Mech* **10:** 463–474. doi:10.1242/dmm.025809

Agoston Z, Heine P, Brill MS, Grebbin BM, Hau A-C, Kallenborn-Gerhardt W, Schramm J, Götz M, Schulte D. 2014. Meis2 is a Pax6 co-factor in neurogenesis and dopaminergic periglomerular fate specification in the adult olfactory bulb. *Development* **141:** 28–38. doi:10.1242/dev.097295

Allen ZJ, Waclaw RR, Colbert MC, Campbell K. 2007. Molecular identity of olfactory bulb interneurons: Transcriptional codes of periglomerular neuron subtypes. *J Mol Histol* **38:** 517–525. doi:10.1007/s10735-007-9115-4

Arnoldini M, Heck T, Blanco-Fernández A, Hammes F. 2013. Monitoring of dynamic microbiological processes using real-time flow cytometry. *PLoS One* **8:** e80117. doi:10.1371/journal.pone.0080117

Barritt GJ. 1999. Receptor-activated Ca^{2+} inflow in animal cells: a variety of pathways tailored to meet different intracellular Ca^{2+} signalling requirements. *Biochem J* **337:** 153–169. doi:10.1042/bj3370153

Berl S, Karram K, Scheller A, Jungblut M, Kirchhoff F, Waisman A. 2017. Enrichment and isolation of neurons from adult mouse brain for ex vivo analysis. *J Neurosci Methods* **283:** 15–22. doi:10.1016/j.jneumeth.2017.03.015

Bito H, Deisseroth K, Tsien RW. 1996. CREB phosphorylation and dephosphorylation: A Ca^{2+}- and stimulus duration–dependent switch for hippocampal gene expression. *Cell* **87:** 1203–1214. doi:10.1016/S0092-8674(00)81816-4

Bustin SA, Benes V, Garson JA, Hellemans J, Huggett J, Kubista M, Mueller R, Nolan T, Pfaffl MW, Shipley GL, et al. 2009. The MIQE guidelines: minimum information for publication of quantitative real-time PCR experiments. *Clin Chem* **55:** 611–622. doi:10.1373/clinchem.2008.112797

Butler A, Hoffman P, Smibert P, Papalexi E, Satija R. 2018. Integrating single-cell transcriptomic data across different conditions, technologies, and species. *Nat Biotechnol* **36:** 411–420. doi:10.1038/nbt.4096

Cadwell CR, Palasantza A, Jiang X, Berens P, Deng Q, Yilmaz M, Reimer J, Shen S, Bethge M, Tolias KF, et al. 2016. Electrophysiological, transcriptomic and morphologic profiling of single neurons using patch-seq. *Nat Biotechnol* **34:** 199–203. doi:10.1038/nbt.3445

Castagnola S, Delhaye S, Folci A, Paquet A, Brau F, Duprat F, Jarjat M, Grossi M, Béal M, Martin S, et al. 2018. New insights into the role of Cav2 protein family in calcium flux deregulation in Fmr1-KO neurons. *Front Mol Neurosci* **11:** 342. doi:10.3389/fnmol.2018.00342

Cazareth J, Guyon A, Heurteaux C, Chabry J, Petit-Paitel A. 2014. Molecular and cellular neuroinflammatory status of mouse brain after systemic lipopolysaccharide challenge: importance of CCR2/CCL2 signaling. *J Neuroinflammation* **11:** 132. doi:10.1186/1742-2094-11-132

Cea-Del Rio CA, Huntsman MM. 2014. The contribution of inhibitory interneurons to circuit dysfunction in fragile X syndrome. *Front Cell Neurosci* **8:** 245. doi:10.3389/fncel.2014.00245

Cheng G-R, Li X-Y, Xiang Y-D, Liu D, Mcclintock SM, Zeng Y. 2017. The implication of AMPA receptor in synaptic plasticity impairment and intellectual disability in fragile X syndrome. *Physiol Res* **66:** 715–727. doi:10.33549/physiolres.933473

Chow S, Patel H, Hedley DW. 2001. Measurement of MAP kinase activation by flow cytometry using phospho-specific antibodies to MEK and ERK: potential for pharmacodynamic monitoring of signal transduction inhibitors. *Cytometry* **46:** 72–78. doi:10.1002/cyto.1067

Contractor A, Klyachko VA, Portera-Cailliau C. 2015. Altered neuronal and circuit excitability in fragile X syndrome. *Neuron* **87:** 699–715. doi:10.1016/j.neuron.2015.06.017

Datta S, Malhotra L, Dickerson R, Chaffee S, Sen CK, Roy S. 2015. Laser capture microdissection: Big data from small samples. *Histol Histopathol* **30:** 1255–1269. doi:10.14670/HH-11-622

Drozd M, Delhaye S, Maurin T, Castagnola S, Grossi M, Brau F, Jarjat M, Willemsen R, Capovilla M, Hukema RK, et al. 2019. Reduction of Fmr1 mRNA levels rescues pathological features in cortical neurons in a model of FXTAS. *Mol Ther Nucleic Acids* **18:** 546–553. doi:10.1016/j.omtn.2019.09.018

Dunne JF. 1991. Time window analysis and sorting. *Cytometry* **12:** 597–601. doi:10.1002/cyto.990120703

Ferron L. 2016. Fragile X mental retardation protein controls ion channel expression and activity. *J Physiol* **594:** 5861–5867. doi:10.1113/JP270675

Fujiwara N, Cave JW. 2016. Partial conservation between mice and humans in olfactory bulb interneuron transcription factor codes. *Front Neurosci* **10:** 337. doi:10.3389/fnins.2016.00337

Fulwyler MJ. 1965. Electronic separation of biological cells by volume. *Science* **150:** 910–911. doi:10.1126/science.150.3698.910

Fuzik J, Zeisel A, Máté Z, Calvigioni D, Yanagawa Y, Szabó G, Linnarsson S, Harkany T. 2016. Integration of electrophysiological recordings with single-cell RNA-seq data identifies neuronal subtypes. *Nat Biotechnol* **34:** 175–183. doi:10.1038/nbt.3443

Giliberti A, Currò A, Papa FT, Frullanti E, Ariani F, Coriolani G, Grosso S, Renieri A, Mari F. 2020. MEIS2 gene is responsible for intellectual disability, cardiac defects and a distinct facial phenotype. *Eur J Med Genet* **63:** 103627. doi:10.1016/j.ejmg.2019.01.017

Goel A, Cantu DA, Guilfoyle J, Chaudhari GR, Newadkar A, Todisco B, de Alba D, Kourdougli N, Schmitt LM, Pedapati E, et al. 2018. Impaired perceptual learning in a mouse model of fragile X syndrome is mediated by parvalbumin neuron dysfunction and is reversible. *Nat Neurosci* **21:** 1404–1411. doi:10.1038/s41593-018-0231-0

Hafemeister C, Satija R. 2019. Normalization and variance stabilization of single-cell RNA-seq data using regularized negative binomial regression. *Genome Biol* **20:** 219. doi:10.1186/s13059-019-1874-1

Holt LM, Olsen ML. 2016. Novel applications of magnetic cell sorting to analyze cell-type specific gene and protein expression in the central nervous system. *PLoS One* **11:** e0150290. doi:10.1371/journal.pone.0150290

Kelley KA. 1989. Sample station modification providing on-line reagent addition and reduced sample transit time for flow cytometers. *Cytometry* **10:** 796–800. doi:10.1002/cyto.990100618

Kilkenny C, Browne WJ, Cuthill IC, Emerson M, Altman DG. 2010. Improving bioscience research reporting: The ARRIVE guidelines for reporting animal research. *PLoS Biol* **8:** e1000412. doi:10.1371/journal.pbio.1000412

La Manno G, Gyllborg D, Codeluppi S, Nishimura K, Salto C, Zeisel A, Borm LE, Stott SRW, Toledo EM, Villaescusa JC, et al. 2016. Molecular diversity of midbrain development in mouse, human, and stem cells. *Cell* **167:** 566–580.e19. doi:10.1016/j.cell.2016.09.027

Le Magueresse C, Monyer H. 2013. GABAergic interneurons shape the functional maturation of the cortex. *Neuron* **77:** 388–405. doi:10.1016/j.neuron.2013.01.011

Li M, Shin J, Risgaard RD, Parries MJ, Wang J, Chasman D, Liu S, Roy S, Bhattacharyya A, Zhao X. 2020. Identification of FMR1-regulated molecular networks in human neurodevelopment. *Genome Res* **30:** 361–374. doi:10.1101/gr.251405.119

Maurin T, Bardoni B. 2018. Fragile X mental retardation protein: to be or not to be a translational enhancer. *Front Mol Biosci* **5:** 113. doi:10.3389/fmolb.2018.00113

Maurin T, Lebrigand K, Castagnola S, Paquet A, Jarjat M, Popa A, Grossi M, Rage F, Bardoni B. 2018. HITS-CLIP in various brain areas reveals new targets and new modalities of RNA binding by fragile X mental retardation protein. *Nucleic Acids Res* **46:** 6344–6355. doi:10.1093/nar/gky267

Maurin T, Melancia F, Jarjat M, Castro L, Costa L, Delhaye S, Khayachi A, Castagnola S, Mota E, Di Giorgio A, et al. 2019. Involvement of phosphodiesterase 2A activity in the pathophysiology of fragile X syndrome. *Cereb Cortex* **29:** 3241–3252. doi:10.1093/cercor/bhy192

Mi D, Li Z, Lim L, Li M, Moissidis M, Yang Y, Gao T, Hu TX, Pratt T, Price DJ, et al. 2018. Early emergence of cortical interneuron diversity in the mouse embryo. *Science* **360:** 81–85. doi:10.1126/science.aar6821

Mientjes EJ, Nieuwenhuizen I, Kirkpatrick L, Zu T, Hoogeveen-Westerveld M, Severijnen L, Rifé M, Willemsen R, Nelson DL, Oostra BA. 2006. The generation of a conditional *Fmr1* knock out mouse model to study Fmrp function in vivo. *Neurobiol Dis* **21:** 549–555. doi:10.1016/j.nbd.2005.08.019

Miyashiro KY, Beckel-Mitchener A, Purk TP, Becker KG, Barret T, Liu L, Carbonetto S, Weiler IJ, Greenough WT, Eberwine J. 2003. RNA cargoes associating with FMRP reveal deficits in cellular functioning in Fmr1 null mice. *Neuron* **37:** 417–431. doi:10.1016/S0896-6273(03)00034-5

Ofengeim D, Mazzitelli S, Ito Y, DeWitt JP, Mifflin L, Zou C, Das S, Adiconis X, Chen H, Zhu H, et al. 2017. RIPK1 mediates a disease-associated microglial response in Alzheimer's disease. *Proc Natl Acad Sci* **114:** E8788–E8797. doi:10.1073/pnas.1714175114

Olmos-Serrano JL, Paluszkiewicz SM, Martin BS, Kaufmann WE, Corbin JG, Huntsman MM. 2010. Defective GABAergic neurotransmission and pharmacological rescue of neuronal hyperexcitability in the amygdala in a mouse model of fragile X syndrome. *J Neurosci* **30:** 9929–9938. doi:10.1523/JNEUROSCI.1714-10.2010

Patel AB, Hays SA, Bureau I, Huber KM, Gibson JR. 2013. A target cell-specific role for presynaptic *Fmr1* in regulating glutamate release onto neocortical fast-spiking inhibitory neurons. *J Neurosci* **33:** 2593–2604. doi:10.1523/JNEUROSCI.2447-12.2013

Paul A, Crow M, Raudales R, He M, Gillis J, Huang ZJ. 2017. Transcriptional architecture of synaptic communication delineates GABAergic neuron identity. *Cell* **171:** 522–539.e20. doi:10.1016/j.cell.2017.08.032

Pollen AA, Nowakowski TJ, Shuga J, Wang X, Leyrat AA, Lui JH, Li N, Szpankowski L, Fowler B, Chen P, et al. 2014. Low-coverage single-cell mRNA sequencing reveals cellular heterogeneity and activated signaling pathways in developing cerebral cortex. *Nat Biotechnol* **32:** 1053–1058. doi:10.1038/nbt.2967

Poulin J-F, Tasic B, Hjerling-Leffler J, Trimarchi JM, Awatramani R. 2016. Disentangling neural cell diversity using single-cell transcriptomics. *Nat Neurosci* **19:** 1131–1141. doi:10.1038/nn.4366

R Core Team. 2018. *R: a language and environment for statistical computing*. R Foundation for Statistical Computing, Vienna. https://www.R-project.org/.

Richter JD, Coller J. 2015. Pausing on polyribosomes: make way for elongation in translational control. *Cell* **163:** 292–300. doi:10.1016/j.cell.2015.09.041

Rosenberg SS, Spitzer NC. 2011. Calcium signaling in neuronal development. *Cold Spring Harb Perspect Biol* **3:** a004259. doi:10.1101/cshperspect.a004259

Rosenberg AB, Roco CM, Muscat RA, Kuchina A, Sample P, Yao Z, Graybuck LT, Peeler DJ, Mukherjee S, Chen W, et al. 2018. Single-cell profiling of the developing mouse brain and spinal cord with split-pool barcoding. *Science* **360:** 176–182. doi:10.1126/science.aam8999

Stuart T, Butler A, Hoffman P, Hafemeister C, Papalexi E, Mauck WM III, Hao Y, Stoeckius M, Smibert P, Satija R. 2019. Comprehensive integration of single-cell data. *Cell* **177:** 1888–1902.e21. doi:10.1016/j.cell.2019.05.031

Tang B, Wang T, Wan H, Han L, Qin X, Zhang Y, Wang J, Yu C, Berton F, Francesconi W, et al. 2015. *Fmr1* deficiency promotes age-dependent alterations in the cortical synaptic proteome. *Proc Natl Acad Sci* **112:** E4697–E4706. doi:10.1073/pnas.1502258112

Tárnok A. 1996. Improved kinetic analysis of cytosolic free calcium in pressure-sensitive neuronal cells by fixed-time flow cytometry. *Cytometry* **23:** 82–89. doi:10.1002/(SICI)1097-0320(19960101)23:1<82::AID-CYTO13>3.0.CO;2-S

Tasic B, Menon V, Nguyen TN, Kim TK, Jarsky T, Yao Z, Levi B, Gray LT, Sorensen SA, Dolbeare T, et al. 2016. Adult mouse cortical cell taxonomy revealed by single cell transcriptomics. *Nat Neurosci* **19:** 335–346. doi:10.1038/nn.4216

Taylor CW. 2002. Controlling calcium entry. *Cell* **111:** 767–769. doi:10.1016/S0092-8674(02)01197-2

Verheije R, Kupchik GS, Isidor B, Kroes HY, Lynch SA, Hawkes L, Hempel M, Gelb BD, Ghoumid J, D'Amours G, et al. 2019. Heterozygous loss-of-function variants of MEIS2 cause a triad of palatal defects, congenital heart defects, and intellectual disability. *Eur J Hum Genet* **27:** 278–290. doi:10.1038/s41431-018-0281-5

Vines A, McBean GJ, Blanco-Fernández A. 2010. A flow-cytometric method for continuous measurement of intracellular Ca^{2+} concentration. *Cytometry A* **77A:** 1091–1097. doi:10.1002/cyto.a.20974

Yang Y-M, Arsenault J, Bah A, Krzeminski M, Fekete A, Chao OY, Pacey LK, Wang A, Forman-Kay J, Hampson DR, et al. 2020. Identification of a molecular locus for normalizing dysregulated GABA release from interneurons in the fragile X brain. *Mol Psychiatry* **25:** 2017–2035. doi:10.1038/s41380-018-0240-0

Zeisel A, Muñoz-Manchado AB, Codeluppi S, Lönnerberg P, Manno GL, Juréus A, Marques S, Munguba H, He L, Betsholtz C, et al. 2015. Cell types in the mouse cortex and hippocampus revealed by single-cell RNA-seq. *Science* **347:** 1138–1142. doi:10.1126/science.aaa1934

Zeisel A, Hochgerner H, Lönnerberg P, Johnsson A, Memic F, van der Zwan J, Häring M, Braun E, Borm LE, La Manno G, et al. 2018. Molecular architecture of the mouse nervous system. *Cell* **174:** 999–1014.e22. doi:10.1016/j.cell.2018.06.021

Zwartz GJ, Chigaev A, Foutz TD, Edwards B, Sklar LA. 2011. A miniature couette to generate shear for flow cytometry: Studying real-time modulation of intracellular calcium in monocytic cells. *Cytom Part J Int Soc Anal Cytol* **79A:** 233–240. doi:10.1002/cyto.a.21027

Received February 25, 2020; accepted in revised form September 23, 2020.